

TOPEX/POSEIDON MICROWAVE RADIOMETER PERFORMANCE AND IN-FLIGHT CALIBRATION

Christopher S. Ruf¹

Stephen J. Keilm²

Bala Subramanya¹

Michael A. Janssen²

Timothy Liu²

submitted to

JGR-Oceans TOPEX/Poseidon Special Issue

on

November 15, 1993

1. Department of Electrical Engineering, The Pennsylvania State University, University Park, PA 16802
2. Jet Propulsion Laboratory, California Institute of Technology, Pasadena, CA 91109

ABSTRACT

Results of the in-flight calibration and performance evaluation campaign for the TOPEX/Poseidon Microwave Radiometer (TMR) are presented. Intercomparisons are made between TMR and various sources of ground truth, including ground based microwave water vapor radiometers, radiosondes, global climatological models, SSM/I data over the Amazon rain forest, and models of clear, calm, sub-polar ocean regions. After correcting for pre-flight errors in the processing of thermal/vacuum data, relative channel offsets in the open ocean TMR brightness temperatures were noted at the ± 1 K level for the three TMR frequencies. Larger absolute offsets of 6-9 K over the rain forest indicated a $\pm 5\%$ gain error in the three channel calibrations. This was corrected by adjusting the antenna pattern correction (APC) algorithm. A 10% scale error in the TMR path delay estimates, relative to coincident radiosondes, was corrected in part by the APC adjustment and in part by a 5% modification to the value assumed for the 22.235 GHz water vapor line strength in the path delay retrieval algorithm. After all in-flight corrections to the calibration, TMR retrieval accuracy for the wet tropospheric range correction is estimated at 0.6-1.6 cm RMS with consistent performance under clear, cloudy, and windy conditions.

1. Introduction

The TOPEX/Poseidon (T/P) satellite is a joint venture by NASA and the French space agency CNES which is designed to produce global maps of ocean surface topology (Stewart *et al.*, 1986). It was launched on August 10, 1992 and began operational data taking on September 23, 1992. The primary instruments on the satellite are two radar altimeters. The TOPEX/Poseidon Microwave Radiometer (TMR) is included to monitor and correct for the electrical range delay (henceforth referred to as *path delay*) of the altimeter radar signal due to water vapor and cloud liquid water in the troposphere. In-flight calibration of the TMR is based on intercomparison studies

between TMR data acquired during the first six months of operation and various sources of "ground truth" which were measured or modeled during satellite overpasses of selected ground sites. The results of those intercomparison studies are presented here.

TMR is a modified version of the Scanning Multichannel Microwave Radiometer (SMMR) which flew on SeaSat and Nimbus-7 (Swanson and Riley, 1980). TMR was restricted to operate at 18, 21, and 37 GHz and only in a nadir viewing direction, which is co-aligned with the radar altimeters, in order to accommodate the T/P mission requirements. The main antenna is a partially offset parabolic reflector with a projected aperture of 79 cm. This results in a footprint diameter on the ground of 43.4, 36.4, and 22.9 km at 18, 21 and 37 GHz, respectively. By comparison, the altimeter footprint is approximately 3 km in diameter. TMR operating characteristics are summarized in Table 1. A block diagram of the instrument is shown in Figure 1. Note in the figure that antenna temperature calibration is performed by alternately switching the input to the radiometer, which is normally connected to the main antenna, either to a smaller antenna pointed into cold space or to an internal matched load at approximately 290 K. This approach is similar to that used by SMMR.

The conversion of raw TMR data into path delay corrections can be broken into three distinct steps. The raw data is first converted into antenna temperatures by the calibration procedure described above. This antenna temperature calibration corrects for drifts in the radiometer gain and bias (Ruf *et al.*, 1993). Secondly, the antenna temperatures are corrected for contributions from the sidelobes of the antenna radiation pattern by a procedure referred to as antenna pattern correction (Janssen *et al.*, 1993). The percentage of power received by the antenna from its on-Earth and off-Earth sidelobes is determined from measurements of the radiation

pattern on a far field antenna range prior to launch. These fractional powers, when combined with estimates of the mean on- and off-Earth brightness temperatures, are subtracted from the antenna temperature, resulting in the brightness temperature referred to the antenna main beam. This brightness temperature calibration is effectively a gain and bias correction to the antenna temperature. Thirdly, brightness temperatures at the three TMR frequencies are converted to path delay estimates by a path delay retrieval algorithm (Keihm *et al.*, 1993). The retrieval essentially inverts the integral equation of radiative transfer to extract the water content of the atmosphere from the measured emissive effects of the water. The water content is then related to the path delay by its refractive properties. Uncertainties in the strength of the water vapor absorption line centered at 22.235 GHz, on which the emissive behavior of the water depends, introduces an uncertainty into the "gain" of the path delay retrieval algorithm.

Because all three of the data processing steps described above are essentially linear operations, gain errors in the antenna and brightness temperature calibration will affect the final path delay estimates in the same way as the line strength uncertainty. Similarly, biases in the calibrated brightness temperatures may be due to errors in either the antenna or the brightness temperature calibration procedures. The in-flight calibration described below estimates the gain and bias errors through intercomparisons with various sources of ground truth. An attempt is also made to identify the sources of these errors, so that the proper step in the calibration procedure can be adjusted accordingly. The intent of this approach is to produce both accurate path delay corrections, for use by the radar altimeters, and accurate brightness temperatures, for use in related research areas. Possible uses for well calibrated nadir viewing brightness temperatures include studies of two vs. three frequency path delay retrieval algorithms, refinements to the model for sea surface

TMR Performance and Cal. - November 5, 1993

excess emissivity as a function of wind speed, and corrections to the water vapor line strength.

This paper is divided into six sections. In section II, the sensitivity of the antenna temperature calibration to varying thermal environments is evaluated. This issue had a significant negative impact on the SMMR performance, and the effectiveness of several modifications to TMR, which were made based on lessons learned from SMMR, is assessed. Section III reviews the various sources of ground truth data used in this study. Included are ground based microwave water vapor radiometer (WVR) and radiosonde measurements, climatological model data, DMSP SSM/I data over the Amazon rain forest, and a reference brightness temperature model for clear, calm, sub-polar ocean regions. Section IV describes the changes which were made in the antenna and brightness temperature calibration procedures to correct for bias and gain errors due to instrument effects. Section V describes the changes which were made in the path delay retrieval algorithm to correct for scale errors due to water vapor line strength uncertainties. Section VI concludes with an overall assessment of the accuracy of the brightness temperature and path delay estimates produced by TMR.

Instrument Thermal Performance

SMMR calibration was adversely affected by large temperature variations in the cold sky waveguide and antenna and in the main antenna feed (Francis, 1987; Milman and Willett 1985). A number of modifications to SMMR were made to reduce the sensitivity to the antenna temperature calibration to the on-orbit thermal environment. Polystyrene radomes were placed in front of both the main antenna feed and the cold sky horns. View maneuvers of the spacecraft were incorporated into the operational orbit to keep TMR on the shade side of the satellite. The cold sky horns

were also positioned on the instrument so as to minimize exposure to direct sunlight. In addition, pre-flight calibration of the models used to correct for the emissive and absorptive effects of the radiometer hardware was more extensive in the case of TMR. A detailed description of the TMR hardware modifications and of the changes in the pre-flight calibration are given by Ruf *et al.* (1993).

A time series of the physical temperature of TMR during the first 6 months of flight is shown in Figure 2. This temperature sensor is located in the heart of the microwave electronics subsystem for the primary 21 GHz channel, and represents a good estimate of the overall temperature of the critical electronics. Extensive pre-flight performance evaluations of TMR were conducted over the range 5-45 C. Second order non-linear instrument response was noted at that time which varied with the physical temperature of the instrument. These effects were modelled in the antenna temperature calibration procedure and make the quality of the calibration slightly dependent on the operating temperature of the instrument (Ruf *et al.*, 1993). The in-flight temperatures are seen to lie comfortably within the pre-flight test range.

Francis (1987) showed that the most significant temperature induced degradation in SMMR performance occurred during the shade-to-sun transition of each orbit. Figure 3a shows a ≈ 0.015 K/s variation in the temperature of the SMMR antenna feed during this time. In contrast, figure 3b shows a ≈ 0.001 K/s temperature variation for TMR during the same transition period. This large reduction in the coupling between incident solar radiation and instrument temperature is due primarily to the incorporation of radomes over the antennas (Linn, 1992).

III. Ground Truth Database

Water Vapor Radiometers

Ground based microwave water vapor radiometers (WVRs) were deployed on the

islands of Lampedusa, Italy (35.57N, 12.57E), Chichi Jima, Japan (27.08N, 142.18E) and Norfolk, Australia (29.03S, 167.93E) and on the oil platform Harvest (34.47N, 239.32E), 11 km from the California coastline. These sites all lie near the satellite ground track. The WVRs deployed at Lampedusa and Harvest operate at 20.7, 22.2, and 31.4 GHz. The single WVR deployed first at Chichi Jima and then at Norfolk operates at 20.7 and 31.4 GHz. All three WVRs achieve an absolute calibration accuracy in their brightness temperature measurements of approximately 0.5 K (Keilm, 1991). This corresponds to an accuracy in the retrieval of path delay of approximately 0.25 cm due to instrument effects alone.

Lampedusa and Harvest are the primary altimeter validation sites for CNES and NASA, respectively. Both sites lie near a crossover point between ascending and descending nodes of the T/P orbit and thus accumulate two near overpasses during each 9.9 day repeat cycle. WVRs were deployed there in part to calibrate TMR and in part to assist with the atmospheric corrections during the altimeter intercomparisons. For these reasons, the Lampedusa and Harvest WVRs have remained in the field and are expected to continue monitoring each overpass for the life of the mission. Norfolk and Chichi Jima were selected as additional temporary WVR sites exclusively for comparison with the TMR. Norfolk lies 29 km from an ascending node ground track and Chichi Jima lies 33 km from an ascending and 50 km from a descending node. A single WVR was deployed first at Chichi Jima during September of 1992, then relocated to Norfolk for comparisons through November 15, 1992. During this time, intercomparison data were obtained for twelve overpasses. Of this data, eleven overpasses occurred under cloud free and light wind (< 7 m/s) conditions.

WVR intercomparisons with the TMR were made primarily between brightness temperatures, since this is the direct measurement made by the WVRs and the comparisons are unaffected by assumptions made regarding the vapor absorption line

strength. Clear, calm conditions were preferred in the intercomparison analysis since cloud effects are highly variable spatially, and windy conditions introduce an added uncertainty into the estimate of the ocean surface contribution to the TMR brightness temperatures. Zenith brightness temperatures measured by the WVR 20.7 GHz channel ranged over 12-52 K for the clear, calm data, corresponding to a variation in path delay of 4-24 cm. From the WVR data, an estimate can be made of the coincident brightness temperature as seen by TMR. This estimate utilizes a well-constrained model for the water vapor line shape and takes into account the temperature and emissivity of the ocean surface. The TMR brightness temperature can be expressed as

$$TB_{TMR} = \epsilon T_s e^{-\tau} + TB_{UP} + (TB_{DN} + T_C e^{-\tau})(1 - \epsilon)e^{-\tau} \quad (1)$$

where ϵ is the calm water emissivity, T_s is the sea surface temperature in K, τ is the atmospheric opacity, TB_{UP} and TB_{DN} are the upwelling and downwelling components of the atmospheric emission, and T_C is the cosmic background brightness temperature. The WVR measurements can be used to predict τ , TB_{UP} , and TB_{DN} at the TMR frequencies. Based on regression fits to computations from a four year Bermuda radiosonde data set, we use

$$\begin{aligned} \tau_{18} &= 0.0113 + 0.00076TB_{WVR21} + 0.00008TB_{WVR22} + 0.00132TB_{WVR31} + 0.00005T_A \\ \tau_{21} &= 0.0688 + 0.00283TB_{WVR21} + 0.00142TB_{WVR22} + 0.00060TB_{WVR31} + 0.00029T_A \\ \tau_{37} &= 0.0546 + 0.00034TB_{WVR21} + 0.00018TB_{WVR22} + 0.00420TB_{WVR31} + 0.00017T_A \end{aligned} \quad (2)$$

$$\begin{aligned} TB_{UP18} &= -2.836 + 0.1832TB_{WVR21} - 0.0338TB_{WVR22} + 0.4418TB_{WVR31} + 0.0029T_A \\ TB_{UP21} &= -1.840 + 1.0492TB_{WVR21} + 0.0907TB_{WVR22} - 0.1265TB_{WVR31} - 0.0014T_A \\ TB_{UP37} &= 2.866 - 0.1362TB_{WVR21} + 0.0351TB_{WVR22} + 1.2143TB_{WVR31} - 0.0096T_A \end{aligned} \quad (3)$$

TMR and Cal 15,

where T_A is the surface air temperature in K and $T_{BWVR,m}$ is the WVR measurement at frequency m ($m = 21$ for 20.7 GHz, $m = 22$ for 22.2 GHz, and $m = 31$ for 31.4 GHz). The residual RMS errors in equation 2 are 0.0004, 0.0023, and 0.0011 for the predicted TMR opacities at 8, 21, and 37 GHz². The errors in equation 3 are 0.041, 0.056, and 0.070 K for the predicted TMR TBUP values. By equating TBPN and TBUP (accurate to 0.1-0.2 K), and using site measurements for T_S and T_A , WVR-predicted TMR brightness temperatures were computed for each ground site overpass using equations 3. The dominant uncertainty in the prediction is due to the uncertainty in the calm sea emissivity ϵ . This issue is discussed in the following sections.

Radiosondes

Fifteen radiosonde launch sites were identified which lie near the T/P ground track and from which weather balloons are generally launched twice daily at 1100 and 2300 UTC. They are listed in Table 2, along with the mean path delay at each site during the first six months of the T/P mission. Individual path delays during each overpass varied over the range 3-40 cm, providing a wide range of conditions for the intercomparison. Since path delay estimates derived from the raw radiosonde measurements have the least sensitivity to modeling errors (as opposed to brightness temperature estimates computed using the equation of radiative transfer), they will be compared directly to the path delay retrieved by TMR. Also included in Table 2 is the distance from the launch site to the satellite ground track at the point of closest approach. Since T/P operates in a non-sun synchronous orbit, the time difference between balloon launch and overpass is fairly uniformly distributed over 0-6 hours. Overpasses for which a launch did not occur within 6 hours were not included in this database.

NCMWP

The French Meteorological Service maintains a dynamic global model of the water vapor and temperature distributions in the atmosphere called NCMW (Jordan *et al.*, 1990). This model is constrained by satellite data and the global network of radiosonde profiles measured twice daily. Spatial interpolation between these boundaries is based on physical models for the atmospheric dynamics. CNRS provides NCMW derived estimates of the path delay in parallel with all TMR data and this archive intercomparison database is available to complement the direct radiosonde intercomparisons described above (Stam, 1993).

DMSP SSM/I

The Special Sensor Microwave/Imager instrument on the Defense Meteorological Satellite Program Block 5D-2 spacecraft provides brightness temperature images at 9.3, 37.0, and 85.5 GHz with vertical and horizontal polarization and at 22.2 GHz with vertical polarization only, all at a constant incidence angle of 53.1°. SSM/I is a mechanically scanning imager with a cross track swath width of 1394 km and resolution of 54, 49, 32, and 14 km at 9.3, 22.2, 37, and 85.5 GHz, respectively. Absolute calibration of the SSM/I brightness temperatures is estimated to be better than ± 3 K for all channels (Dollinger *et al.*, 1990). SSM/I measurements were used to identify regions of the Amazon rain forest which could be assumed to be approximate black body targets. This was done by requiring that there be a sufficiently small difference between the vertically and horizontally polarized brightness temperatures. Average SSM/I brightness temperatures over these regions were then compared to the average TMR brightness temperatures. SSM/I estimates of integrated water vapor over the open ocean were not intercompared with TMR rainfall

delays due to the unacceptably large temporal decorrelation of the path delay fields between the two data sets.

Intercomparisons of SSM/I with TMR concentrated on days 278-290 of 1992. A number of SSM/I passes in the region of the Amazon rain forest were examined. It was found that a significant percentage of the data lying within $0-10^{\circ}$ south latitude and $60-70^{\circ}$ west longitude had little polarization signature. Specifically, ascending passes were examined on day 281 at 01:03-01:09 UTC (corresponding to $0-10^{\circ}\text{S}$, $61.3-63.6^{\circ}\text{W}$) and day 287 at 01:16-01:22 UTC ($0-10^{\circ}\text{S}$, $64.4-66.7^{\circ}\text{W}$). Descending passes were examined on day 282 at 13:09-13:15 UTC ($0-10^{\circ}\text{S}$, $64.4-66.6^{\circ}\text{W}$) and day 285 at 13:15-13:22 UTC ($0-10^{\circ}\text{S}$, $66.0-68.0^{\circ}\text{W}$). All points were extracted for which the vertical and horizontal brightness temperatures at 19.3 and 37.0 GHz differed by less than 1.0 K. The results are summarized in Table 3.

A small increase in the mean brightness temperature is evident from night to day, but not enough to be explained simply by the typical day and night air temperatures in the region. For example, the mean daily high (day time) and low (night time) surface air temperatures in Manaus, Brazil (3°S , 60°W) for August-December are 306 and 297 K, respectively (National Geographic, 1990). The effective radiating temperature of the rain forest is apparently lower, relative to the surface air temperature, during the day than it is at night. This can be explained by the increase in altitude during the day (and, hence, the decrease in temperature) of a significant fraction of the atmospheric absorption.

Reference Models

Two models were developed to estimate the hottest and coldest brightness temperatures which TMR was expected to encounter in-flight. The hot model is the Amazon rain forest discussed above. Regions of the rain forest with essentially

unity emissivity were identified using SSM/I data. The expected TMR brightness temperatures in these regions can be expected to be slightly lower than the SSM/I values since the atmosphere is more transparent along TMR's nadir path and the land emission is less completely attenuated.

The coldest brightness temperatures which TMR is expected to encounter occur over open ocean in the sub-polar regions under clear, calm conditions. Sub-polar locales typically provide the lowest atmospheric water vapor content. Clear conditions remove any emissive contributions from clouds, and calm conditions minimize the excess emissivity generated by ocean surface roughness and foaming. Fortunately, the coldest brightness temperatures are also the easiest to model accurately. TMR brightness temperatures were simulated for typical sub-polar conditions using a number of guidelines. The atmospheric dependence was estimated using a four year archive of radiosonde profiles from St. Paul Island (57.2N, 170.2W). The surface emissivity of the ocean was modeled using the Fresnel reflection coefficient and including sea surface salinity and temperature effects on the complex dielectric constant of the water (Klein and Swift, 1978). Sea surface temperature as a function of latitude was derived from regression fits to global AVHRR/2 maps of the ocean during September and October 1987 (Halpern *et al.*, 1992). These months were chosen to coincide with the time of TMR intercomparison. Results of the regression fit follow

$$T_S = 274 + 0.6*(60 - LAT) \quad \text{for southern latitudes} \quad (4)$$

$$T_S = 280 + 0.4*(60 - LAT) \quad \text{for northern latitudes}$$

where T_S is the sea surface temperature in K and LAT is the (positive) latitude in deg. Equation 4 is valid over the range $40 \leq LAT \leq 60$. Clear, calm brightness

temperatures were computed with variable T_S for the range of atmospheric conditions determined by the St. Paul Island archive. These brightness temperatures (T_{Bff} at frequency ff GHz) were then regressed against the path delay (PD) associated with each radiosonde profile and against the assumed sea surface temperature, T_S . The results follow

$$TB18 = 122.53 + 0.652*PD - 0.176*T_S \quad (5)$$

$$TB21 = 126.90 + 2.155*PD - 0.245*T_S$$

$$TB37 = 154.53 + 0.755*PD - 0.509*T_S$$

where PD is in units of cm and T_S in units of C. The RMS residual error between the true brightness temperatures and those predicted by the regression fits was ≤ 0.5 K at all frequencies over the range of conditions $0 < PD \leq 7$ cm and $0 \leq T_S \leq 15$ C. The lowest brightness temperatures, associated with the lowest path delays estimated by TMR (typically 2-3 cm), should correspond with the values predicted by equation 5. This check is useful because the TMR path delay retrieval algorithm tends to produce meaningful (algorithm errors < 1 cm) path delay estimates even when there is a substantial bias in the brightness temperatures, provided the bias is approximately common to all three frequencies (Keihm *et al.*, 1993). Thus, satisfactory path delay intercomparisons alone cannot necessarily guarantee accurate brightness temperature calibration. It should also be noted that uncertainties in the water vapor line strength will have only a minimal effect on the accuracy of the brightness temperatures predicted by equation 5. Errors in the line strength amount to relative errors in the component of the brightness temperature due to the water vapor. Thus, for a condition of $PD = 7$ cm, uncertainty in the line strength at the 5% level will result in TB model errors of only $\approx 0.2, 0.8$, and 0.3 K at 18, 21, and 37 GHz.

IV. Corrections to Instrument Calibration

Bias Correction

Initial intercomparisons between TMIR and the various sources of ground truth immediately after launch indicated very large biases (6-12 K over the three frequencies) in the brightness temperatures. The biases were generally consistent using each of the sources of ground truth. For example, the lowest brightness temperatures measured by TMIR (in the sub-polar regions) were 6-2 K lower than the lowest physically possible values, as determined from equation 5. Likewise, WVR-predicted TMIR brightness temperatures at somewhat higher levels were also 6-12 K above those measured by TMIR. The source of a significant portion of the bias was identified as processing errors in the pre-flight thermal/vacuum (TVV) data analysis. Two problems with the original reduction of the TVV data were corrected. The

thermistor calibration coefficients used to measure the temperature of the cold sky calibration horn target were incorrect. Using the correct coefficients raised the cold sky target temperature by several degrees but did not account for the large biases in the in-flight brightness temperatures. However, this correction has been made in the revised processing reported here. Part of the TVV data, which was used to calibrate the instrument's sensitivity to the cold sky brightness temperature, was found to be unusable due to large temperature gradients present in the cold sky target. This problem was determined to be accountable for almost all of the bias seen in the flight data at the lower end of the range of brightness temperatures. It was corrected by identifying other TVV data taken when the cold sky target was at a stable temperature.

TVV data processing requires that a number of free parameters, associated with the losses and reflections in the on-board TMIR calibration hardware, be estimated

using a multi-linear regression fit to T/V data taken under a wide range of operating temperatures and temperature gradients (Ruf *et al.*, [1993]). A useful figure of merit for the regression fit is the RMS residual error between the antenna temperature measured by TMR and the physical temperature of a target absorber placed over the feed horn of the radiometer. With the revised T/V processing, the RMS error is 0.24, 0.24 and 0.19 K at 18, 21, and 37 GHz. This represents the accuracy of the antenna temperature calibration algorithm for tracking variations in temperature of the absorber target. It doesn't necessarily measure the overall accuracy of the antenna temperature calibration in-flight. Small errors can be expected to result from such effects as backlobe contributions to the antenna feed, non-unity emissivity of the absorber target, and differences between the arithmetic average of the temperature sensors installed in the absorber and the beam-averaged effective radiating temperature of the absorber. It is these errors which the in-flight comparisons are intended to correct.

After revision of the T/V processing, biases in the TMR brightness temperatures, as inferred from the WVR data, were reduced to +0.6 K (TMR low), -0.7 K (TMR high), and -0.1 K (TMR high) at 18, 21, and 37 GHz. These values are derived from the average of 17 overpasses of WVR sites for which the skies were clear, the winds were ≤ 7 m/s, and horizontal variations in the TMR TB measurements were minimal. A scatter plot of the intercomparison data between the WVR-predicted TMR brightness temperature and the TMR data itself (prior to the final gain correction) is shown in Figure 4. These biases have been incorporated into the antenna temperature calibration algorithm as constant offsets. Their significance pertains to the relative channel-to-channel corrections which most directly impact the path delay retrieval algorithm. The derived individual channel absolute offsets are uncertain to a level of a few Kelvin due to uncertainty in the effective emissivity of the calm

sea. The derived relative offsets, however, are much less affected by the emissivity modeling uncertainty. Application of the final instrument gain corrections (described in the following section) yields TMR brightness temperatures which are elevated 2-3 K above the calm sea model predictions. The authors conjecture that this may be due not to errors in TMR calibration, but rather to a deficiency in the model used for the ocean surface emissivity. The ocean surface is modeled as a perfect dielectric half space, with emissivity determined solely by the Fresnel reflection characteristics at the interface. There is some evidence that the true ocean surface emissivity never drops down all the way to the ideal Fresnel condition, even under calm wind, "glassy", conditions (Stogryn, 1967; Bessalova *et al.*, 1981; Gaydinskiy *et al.*, 1988). In addition, inconsistencies have been noted between various models for the dependence of the dielectric constant of ocean water on temperature and salinity (Wentz, 1992). These issues all point to an uncertainty in the calm water emissivity of the ocean which could account for the 2-3 K discrepancy observed here. Constraints on the calm sea emissivity, based on TMR/WVR comparisons, will be explained further using a full year of ground truth data (Keilum and Ruf, 1993)

Gain Correction

A significant gain error was indicated by all pertinent sources of ground truth. These sources can be divided into two classes, path delay and brightness temperature measurements. Comparisons between TMR and either the radiosonde or the ECMWF data revealed relative errors in path delay of $\sim 10\%$. These errors increased with increasing path delay, with TMR estimates of path delay becoming increasingly low. Scatter plots of TMR path delay against radiosonde and ECMWF path delay with this relative error are shown in figure 5. As noted above, possible causes of path delay

relative errors include both water vapor line strength errors and instrument calibration gain errors.

The instrument gain error component was determined by evaluation of the highest TMR brightness temperatures, at which gain errors have the largest effect. Comparisons between the Amazon rain forest black body SSM/I brightness temperatures and the TMR measured brightness temperatures were made by averaging TMR data into eight bins. The TMR data over days 278-290 of 1992 were separated into four latitude and longitude regions: 1) 0-5S, 65-70W; 2) 5-10S, 65-70W; 3) 0-5S, 60-65W; and 4) 5-10S, 60-65W. Data over each region was additionally separated into day (06:00-18:00 local time) and night (18:00-06:00 local time) overpasses. The brightness temperature measurements over each bin are summarized in Table 4. The differential polarization technique used to identify black body regions of the rain forest with the SSM/I data cannot be used here since TMR operates with a single polarization and in the nadir direction at which the land emission is unpolarized. However, the standard deviation of the TMR brightness temperatures over each bin gives some indication of land contamination, since most variability in the brightness temperature can be assumed to come from the surface. For this reason, the (5-10S, 65-70W) region in Table 4 is judged to be most uniformly black body in behavior. Furthermore, the standard deviations at night tend to be approximately equal to or less than those in the day for all four regions. This can be explained as a corollary to the day/night discussion given above regarding the SSM/I rain forest data, for which the effective radiating temperature of the atmosphere is more closely coupled to the surface air temperature during the night. In the case of TMR measurements, the night time air can be regarded as less variable over the ranges of latitude and longitude considered. For these reasons, the (5-10S, 65-70W) night time data will be used as the TMR point of comparison with the SSM/I data.

Comparisons between the specified averaged TMR and SSM/I rain forest data reveal offsets of 9.1, 8.5, and 6.1 K (TMR low) at 18, 21, and 37 GHz. (Here, we have assumed that the 18/19.3 and 21/22.2 brightness temperatures are equal, since the near unity emissivity of the rain forest allows the water vapor absorption spectrum to have only a weak effect on the brightness temperature.) Using the sub-polar model intercomparison as a tie point for the TMR gain calibration, this indicates an instrument gain error of 5.6, 5.3, and 4.6% at 18, 21, and 37 GHz. Several points of qualification should be noted regarding this analysis. The sub-polar model tie point is based on an ideal Fresnel condition at the ocean surface and so may be in error by 1-3 K, as noted above. The assumed equivalence of SSM/I and TMR rain forest measurements may not be exact since the SSM/I antenna beam travels through significantly more atmosphere in its off-nadir orientation. Also, the absolute calibration of SSM/I brightness temperatures has uncertainties of ± 3 K, as noted above. All of these factors combine to make the hot (rain forest) and cold (sub-polar) calibration points uncertain at the 3-5 K level. However, since these points are 132-164 K apart at the three frequencies, the estimates given here for instrumental gain error can be conservatively regarded as accurate within approximately $\pm 2.5\%$.

Regarding the cause of the instrument errors, the very low RMS residuals remaining in the T/V test of the antenna temperature calibration suggest that the brightness temperature calibration is a more likely source of the $\approx 5\%$ gain error. The pre-flight antenna pattern correction coefficients, as determined from antenna range measurements of the TMR sidelobe levels, directly affect the gain of the instrument calibration. The gain is most sensitive to the fraction of the integrated sidelobes which lies off the Earth (outside of 55° off nadir). An underestimate of this beam fraction would result in an overestimate of the instrument sensitivity to

changes in brightness temperature in the nadir direction, since a larger fraction of the beam would then be directed toward nadir. The pre-flight off-Earth beam fractions were estimated at 0.49, 0.29, and 0.37% at 18, 21, and 37 GHz (Janssen *et al.*, 1993). These values have been revised to produce the $\pm 5\%$ gain corrections derived above, and to account for approximately half of the 10% gain error in path delay retrievals. The corrected off-Earth beam fractions are 2.03, 2.04, and 1.77%. The most likely cause of this rise in the integrated power pattern beyond the Earth is a last minute modification to the antenna, made prior to launch but after the antenna range measurements were completed. A full satellite thermal balance test in the TVV chamber indicated that the thermal blanketing of TMR was inadequate. Thermal blankets were added around the collar containing the main reflector's multifrequency feed. These blankets altered the aperture field distribution because the main reflector is only partially offset. The blankets also probably increased the scattering of energy into the far sidelobes of the antenna pattern. While every reasonable effort was made to conform the blankets as closely as possible to the existing feed collar, the increase in power scattered into the far sidelobes is not unexpected.

V. Corrections to Path Delay Algorithm Line Strength Model

The remaining 5% relative path delay error between TMR and the radiosonde and ECMWF ground truth was corrected by adjusting the strength of the water vapor absorption line. The pre-launch absorption model was based on a modification of the Liebe and Layton (1987) model which utilizes the Van Vleck-Weiskopf line shape. The modification was an 8% increase in the model line strength to match comparison data between radiosondes and WVRs (Keilm, 1992) and to match the only available laboratory data which measured the 22.235 GHz absorption feature (Becker and Autler, 1946). The

accuracy of radiosonde calibration of the water vapor absorption feature has long been questioned due to uncertainties in the radiosonde relative humidity measurements, especially at the high and low ends of humidity conditions (Elliot and Gaffen, 1991; Schwartz and Doswell, 1991). Resultant estimates of the vapor absorption model accuracy based on radiosonde/WVR comparisons have been in the 5-10% range. There is also evidence of non-linearities in the absorption vs. vapor density relationship (Hogg and Guiraud, 1979). It is therefore quite plausible that our pre-launch model for vapor absorption may be 5% high, producing TMR path delay results which are 5% low. We have therefore revised our absorption model, lowering the line strength by 5%, to eliminate the remaining scale error indicated by the TMR/radiosonde and TMR/ECMWF comparisons. The resulting model is equivalent to that of Liebe and Layton (1987) with a 3% increase in line strength.

It should be pointed out that the entire 10% scale error apparent in the TMR vs. ground truth path delay comparisons could have been corrected by a 10% decrease in the assumed absorption model. However, to produce the best possible TMR calibrations in terms of both brightness temperatures and path delay, the correction was split equally between the brightness temperature calibration and the path delay algorithm. As discussed previously, the $\approx 5\%$ instrument gain corrections produce consistency between the TMR and SSM/I brightness temperature measurements of the Amazon rain forest.

VI. Conclusions - Assessment of Brightness Temperature and Path Delay Retrieval Accuracies

Brightness Temperature Accuracy

A quantitative measure of the accuracy of the TMR brightness temperature calibration can be made by comparison with the coincident WVR measurements. Unfortunately, the estimated TMR accuracy can not easily be separated from the 1-3 K

uncertainties in the calm sea surface emissivity model. Scatter plots of WVR inferred TMR brightness temperatures against those measured by TMR, after all the calibration corrections have been made, are shown in Figure 6a-c for the three TMR frequencies. The bias between the two data sets is 2.3, 2.9, and 2.2 K, with the TMR high at 18, 21, and 37 GHz. Similar biases (2.8, 3.1, and 3.1 K) are observed when comparing the final TMR calibration to the sub-polar reference models. The success of the revised TVV calibration, instrument gain corrections, and modified path delay retrieval algorithm in producing agreement with both the Amazon brightness temperature data and the ground-based path delay results suggests that the open ocean offsets seen in the brightness temperature comparisons are due to a calm sea component which adds ≈ 0.01 to the Fresnel prediction of the nadir emissivity. As discussed above, previous theoretical and experimental results have suggested the existence of a small 1-3 K non-specular component of the calm sea nadir flux. However, to the authors' knowledge, no previous aircraft or satellite radiometer has demonstrated the absolute calibration accuracy necessary to definitively measure this effect. The TMR data suggests that the calm sea enhancement is 2-3 K over the 18-37 GHz frequency range. This result depends primarily on the accuracy of our SSM/I-based model for the Amazon rain forest emission. Assuming that the derived gain corrections may be in error by up to $\pm 2.5\%$, we estimate the TMR open ocean brightness temperature accuracy to be ± 1.5 K.

Path Delay Accuracy

The accuracy of TMR retrievals of path delay is derived primarily from a comparison with the radiosonde database. A scatter plot of TMR and radiosonde path delays is shown in figure 7 after all instrument calibration and water vapor line strength corrections have been incorporated into the TMR data processing. This data

set includes clear, calm weather conditions as well as all cloudy and windy cases experienced during the first 6 months of the mission. The RMS scatter between the two data Sets is 3.0 cm. This scatter includes three uncorrelated sources in addition to the TMR error. The RMS error associated with individual radiosonde soundings is estimated to be 0.8 cm (Alishouse *et al.*, 1990). The RMS spatial decorrelation between the footprint averaged TMR path delay and the point measurement made by the radiosonde is estimated at 2.0 cm. This estimate is based on a correlation analysis of the spatial variability of the TMR data and a determination of the mean radiosonde-groundtrack separation. The RMS temporal decorrelation between the time of TMR overpass and the nearest radiosonde launch has been estimated at 1.3-2.0 cm. This estimate assumes that spatial and temporal decorrelation can be related by the horizontal motion of the path delay field due to wind. The range given depends on the relative alignment of the local wind vector and the satellite ground track. This results in an RMS error for the TMR path delay retrieval in the range 0.6-1.6 cm. Further refinement of this TMR error budget would require a careful analysis of the temporal decorrelation statistics and is not planned at present.

Path Delay Sensitivity to Clouds and Wind

The mission requirements for TMR included the ability to accurately retrieve path delay under all cloudy and windy conditions, excluding rain. This can be readily demonstrated, since the TMR retrieval algorithm also estimates ocean surface wind speed and integrated cloud liquid water content along with each path delay estimate. (These parameters are used as second order corrections to the path delay retrieval algorithm itself (Keihm *et al.*, 1993).) The difference between radiosonde and TMR path delay is plotted against the wind speed and cloud liquid retrieved by

TMR, in figures 8a and 8b. A summary of the RMS scatter and mean difference between the radiosonde and TMR values is given in Table 5 for different subsets of the wind and cloud liquid retrievals. The figure and table indicate that the RMS accuracy of the TMR path delay retrieval is relatively insensitive to the cloud and wind conditions, thus satisfying the mission requirements. Table 5 also indicates that TMR path delay is not significantly biased under consistently windy or cloudy conditions. This is in marked contrast to the path delay retrieval performance predicted for several two frequency retrieval algorithms (Keihm *et al.*, 1993). For example, biases of 2-5 cm are predicted by Keihm *et al.* (1993) with a satellite water vapor radiometer operating at 21 and 37 GHz under surface wind speed conditions of 18-28 m/s. The issue of how many (and which) frequencies are needed to retrieve path delay satisfactorily is timely in light of the current design studies underway for TOPEX Follow On, GEOSAT Follow On II, the EOS Altimeter radiometer, and the ERS-1 Follow On radiometer. The presence of large biases in the two frequency retrieval algorithms does not significantly increase the global RMS error in the path delay retrieval, since high wind conditions happen relatively infrequently on a global scale. However, such path delay retrieval algorithms, which are designed to minimize global RMS error, can introduce artifacts into the ocean surface topology maps in isolated regions of the globe over which mean surface winds are anomalously high.

ACKNOWLEDGMENTS

The authors would like to acknowledge the assistance of several individuals and organizations for their assistance with this work. Drs. Peter Gaiser and Karen St. Germain of the University of Massachusetts operated the WVRs at Chichi Jima and Norfolk Island. The Japanese Local Meteorological Observatories and the Australian Bureau of Meteorology were very helpful in facilitating the WVR deployments at Chichi

Jima and Norfolk Island. Dr. Alan Tanner of the Jet Propulsion Laboratory maintained the WVRs at Harvest and Lampedusa. Ms. Dawn Conway of the Naval Research Laboratory helped with the extraction of pertinent SSM/I data from NRL's DMSP archive. This work presents the results of one phase of research conducted at the Jet Propulsion Laboratory, California Institute of Technology, Pasadena, CA, under contract to the National Aeronautics and Space Administration.

REFERENCES

- Alishouse, J.C., S.A. Snyder, J. Vongsathorn, and R.R. Ferraro (1990), *Determination of oceanic total precipitable water from the SSM/I*, IEEE Trans. Geoscience Remote Sens., Vol. 28, No. 5, pp. 811-816.
- Becker, G.E. and S.H. Autler (1946), *Water vapor absorption of electromagnetic radiation in the centimeter wavelength range*, Phys. Rev., Vol. 70, 300-307.
- Bezpalkova, Y.A., V.M. Veselov, A.A. Glotov, Y.A. Milinski, V.G. Mirovskiy, L.V. Pokrovskaya, A.Y. Popov, M.D. Rayev, E.A. Sharkov, and V.S. Etkin (1981), *Sea-ripple anisotropy estimates from variations in polarized thermal emission of the sea*, translated from the Russian in Oceanology, Scripps Publishing Company.
- Elliot, W.P. and D.J. Gaffen (1991), *On the utility of radiosonde humidity archives for climate studies*, Bull. Amer. Meteorol. Soc., Vol. 72, 1507-1520.
- Francis, E.A. (1987), *Calibration of the Nimbus 7 SMMR*, M.S. Thesis, Dept. of Oceanography, Oregon State Univ., Corvallis, OR, 248 pp.
- Gaydanskiy, S.I., V.Y. Gershenzon, and V.K. Gromov (1988), *Detection of surface manifestations of internal waves in the ocean by microwave radiometry*, Izvestiya, Atmos. Ocean. Physics, Vol. 24, 731-735.
- Halpern, D., V. Slotnicki, J. Newman, D. Dixon, O. Brown, and E. Wentz (1992), *An atlas of monthly mean distributions of GEOSAT sea surface height, SSM/I surface*

- wind speed, AVHRR/2 sea surface temperature, and ECMWF surface wind components during 1987, Jet Prop. Lab. Pub. No. 92-3.
- Hogg, D.C. and F.O. Guiraud (1979), *Microwave measurements of the absolute values of absorption by water vapour in the atmosphere*, Nature, Vol. 279, 408-409.
- Hollinger, J.P., J.L. Pierce, and G.A. Poe (1990), *SSM/I Instrument Evaluation*, IEEE Trans. Geoscience Remote Sens., Vol. 28, No. 5, 781-790.
- Janssen, M.A., C.S. Ruf, and S.J. Keihm (1993), *TOPEX/POSEIDON Microwave Radiometer (TMR): II. Antenna pattern correction and brightness temperature algorithm*, submitted for publication in IEEE Trans. Geoscience Remote Sens.
- Jourdan, D., C. Boissier, A. Braun, and J.F. Minster (1990), *Influence of wet tropospheric correction on mesoscale dynamic topography as derived from satellite altimetry*, J. Geophys. Res., 95, C10, 17993-18004.
- Keihm, S.J. (1991), *Water vapor radiometer intercomparison experiment: Platteville, Colorado, March 1-14, 1991*, Final report prepared for Battelle, Pacific Northwest Laboratories, on Behalf of the Department of Energy, Jet Prop. Lab. Doc. No. D-8898.
- Keihm, S.J. (1992), *Atmospheric absorption from 20-32 GHz: Radiometric constraints on the vapor and oxygen components*, Proceedings of Specialist Meeting on Microwave Radiometry and Remote Sensing Applications, (E.R. Westwater, ed.), Boulder, Colorado, 211-218.
- Keihm, S.J., M.A. Janssen, and C.S. Ruf (1993), *TOPEX/POSEIDON Microwave Radiometer (TMR): III. Wet troposphere range correction algorithm and pre-launch error budget*, submitted for publication in IEEE Trans. Geoscience Remote Sens.
- Keihm, S.J. and C.S. Ruf (1993), *The role of water vapor radiometers in the TOPEX Microwave Radiometer in-flight calibration*, in preparation for submittal to Journal of Marine Geodesy.

- Klein, L.A. and C.T. Swift (1977), *An improved model for the dielectric constant of sea water at microwave frequencies*, IEEE J. Oceanic Eng., OE-2, 104-111.
- Liebe, H.J. and D.H. Layton (1987), *Millimeter-wave properties of the atmosphere: Laboratory studies and propagation modeling*, Nat. Technol. and Inform. Admin., Boulder, CO, NTIA Rep. 87-24.
- Linn, E.L. (1992), *TOPEX Microwave Radiometer: Thermal design verification test and analytical model validation*, AIAA 30th Aerospace Sciences Meeting and Exhibit, Reno, NV, AIAA 92-0816.
- Milman, A.S. and T.T. Wilheit (1985), *Sea surface temperature from the Scanning Multichannel Microwave Radiometer on Nimbus 7*, J. Geophys. Res., 90, C6, 11, 631-11, 641.
- National Geographic Atlas of the World (1990), 6th ed., National Geographic Society, Washington, D.C.
- Ruf, C.S., S.J. Keihm, and M.A. Janssen (1993), *TOPEX/POSEIDON Microwave Radiometer (TMR): I. Instrument description and antenna temperature calibration*, submitted for publication in IEEE Trans. Geoscience Remote Sens.
- Schwartz, B.E. and C.A. Doswell III (1991), *North American rawinsonde observations: Problems, concerns, and a call to action*, Bull. Amer. Meteorol. Soc., Vol. 72, 1885-1896.
- Stewart, R., L.-L. Fu, and M. Lefebvre (1986), *Science opportunities from the TOPEX/Poseidon mission*, Rep. 86-18, Jet Propul. Lab., Pasadena, Calif.
- Stogryn, A. (1967), *The apparent temperature of the sea at microwave frequencies*, IEEE Trans. Antennas Propagat., Vol. AP-15, pp. 278-286.
- Stum, J. (1993), *A comparison between TOPEX Microwave Radiometer, ERS-1 microwave radiometer and ECMWF derived wet tropospheric corrections*, J. Geophys. Res. - Oceans, this issue.

- Swanson P.N. and A.L. Riley (1980), *The SeaSat Scanning Multichannel Microwave Radiometer (SMMR): Radiometric calibration algorithm development and performance*, IEEE J. Ocean. Engin., OI-5, 2, 116-124.
- Wentz, F.J. (1992), *Measurements of Oceanic Wind Vector Using Satellite Microwave Radiometers*, IEEE Trans. Geoscience Remote Sens., Vol. 30, pp. 960-972

TABLE 1 TMR Engineering Specifications

FREQUENCY (GHz)	18	21A	21B	37
HPBW (deg)	1.86	1.56	1.59	0.98
Footprint (km)	43.4	36.4	37.1	22.9
beam Efficiency (%)	91.1	89.3	87.4	90.5
Integration Time (s)	1.0	1.0	1.0	1.0
Radiometer Noise, ΔT (K)	0.26	0.27	0.27	0.27
1A Accuracy (K) ²	0.57	0.57	0.54	0.54
Pre-flight 1B Accuracy (K) ³	0.77	0.74	0.79	0.71
In-flight 1B Accuracy (K)	1.5	1.5	1.5	1.5

NOTE: 1. Channel 21B is a redundant backup channel. It was not used during the verification mission.

2. Antenna temperature calibration accuracy does not include the antenna pattern corrections (Ruf *et al.*, 1993)
3. Pre-flight brightness temperature accuracy refers to the predicted TMR performance, assuming representative antenna pattern measurements (Janssen *et al.*, 1993). The addition of thermal blanketing around the antenna feed prior to launch necessitated in-flight adjustments to the far sidelobe levels, which introduced additional uncertainties into the brightness temperature calibration algorithm.

TABLE 2. Radiosonde Intercomparison Database

Station Name	LAT (N)	LONG (E)	AVG PD (cm)	Closest Approach (km)
PORT BLAIR	11.67	92.72	24.5	9.1
JIACHUOJIMA	33.10	139.78	10.4	40.1
NAZE-ON-AMAMI	28.38	129.50	13.4	14.1
NAHA	26.12	127.40	16.6	19.2/42.6
MINAMIDAITOJIMA	25.83	131.23	11.4	31.1
CHICHIJIMA	27.08	142.18	15.7	32.8/49.9
MINAMITORISHIMA	24.30	153.97	18.4	29.8
GOUGH ISLAND	-40.35	-9.88	12.5	42.5/49.6
MARION ISLAND	-46.88	37.87	13.3	25.6
Sri. PAUL ISLAND	57.15	-170.22	6.3	36.7/48.3
SABLE ISLAND	43.93	-60.02	7.3	11.1
BERMUDA IN A};	32.37	-64.68	15.0	43.8/44.4
JULIANA AIRPORT	18.05	-63.12	18.1	31.8
GRANTLEY ADAMS	13.07	-59.48	24.0	15.0/25.2
ANDERSEN AFB GUAM	13.33	144.50	19.2	26.4/27.7

NOTE: Closest approach values are distances from satellite ground track to radiosonde launch site. Double values indicate that both ascending and descending orbit nodes come within 100 km of the site.

TABLE 3. SSM/I Blackbody Brightness Temperatures in Amazon Rain Forest

Day of year 1992	Local time	TB : Mean \pm Std. dev.			# of points
		19.3 GHz	22.2 GHz	37 GHz	
281	22:06	285.1 \pm 2.2	283.4 \pm 2.3	281.1 \pm 2.5	1506
282	10:12	286.2 \pm 1.9	284.4 \pm 1.8	282.8 \pm 1.8	1722
285	10:18	286.7 \pm 2.3	284.7 \pm 2.2	283.1 \pm 2.3	1883
287	22:19	285.3 \pm 1.8	284.1 \pm 1.8	281.6 \pm 2.0	1571
Average		285.8	284.2	282.2	

NOTES: 1. Blackbody condition defined as $|TB_v - TB_h| \leq 1.0$ K for both 19.3 and 37.0 GHz.

2. See text for description of latitude and longitude ranges for each of these four passes.

TABLE 4. TMIR TBs in Amazon Rain Forest Before Gain Correction

LAT/LON range	Day/Night	18 GHz TB: Mean \pm Std. dev.	24 GHz	37 GHz	# of points
0-5S, 65-70W	Day	272.914.2	273.343.1	273.544.3	90
0-5S, 65-70W	Night	273.242.6	273.344.9	273.743.0	58
5-10S, 65-70W	Day	273.740.8	273.640.8	274.140.9	92
5-10S, 65-70W	Night	276.741.2	275.741.0	276.141.5	94
0-5S, 60-65W	Day	265.247.4	267.145.8	267.747.0	78
0-5S, 60-65W	Night	272.145.0	273.943.4	273.944.4	47
5-10S, 60-65W	Day	273.342.7	272.742.1	273.742.9	93
5-10S, 60-65W	Night	275.342.6	276.442.2	276.643.2	47

NOTES: Data extracted from days 278-290 of 1992.

2. Day range is 06:00-18:00 local time; Night range is 18:00-06:00 local time.

3. TMIR brightness temperatures calibrated assuming mean on-140th for sidelobe brightness temperature of 280 K (Janssen *et al.*, 1993).

TABLE 5. TMR Path Delay Sensitivity to Clouds and Wind

Wind speed range (m/s)	Cloud liquid range (microns)	(Radiosonde - TMR Path Delay)		
		RMS	Average	# of samples
ALL	ALL	3.00	0.44	268
<8	ALL	3.34	0.12	74
8-15	ALL	2.83	0.62	15s
>15	ALL	3.01	0.28	36
ALL	<50	3.21	0.53	152
ALL	50-300	2.85	0.02	94
ALL	>300	2.00	-0.32	22

NOTES: 1. Wind speed and cloud liquid are retrieved from TMR brightness temperatures by statistical inversion. The absolute accuracy of these retrievals has not been independently verified, but their performance is expected to be sufficient to differentiate the general classes of weather conditions considered here.

2. RMS and average statistics of the TMR path delay error are based on the data set described in figure 5.

FIGURES CAPTIONS

figure 1 TMIR functional Block Diagrams. (A) System design and () Typical radiometer channel.

Figure 2. Time series of TMIR instrument temperature during the first 6 months of the mission.

figure 3. Time series of front-end microwave components critical to the antenna temperature calibration during one orbit. (A) Main reflector feed horn on the Nimbus 7 SMMR for a number of different orbits over the course of the mission (from Francis, 1987). (B) Feed horn, cold sky (cal) horn, and cal horn waveguide on TMIR for one typical orbit. The largest temperature changes occur during the shade-to-sun transition in the orbit, at $0-45^\circ$ ecliptic angle for SMMR and at 60-165 min for TMIR. Temperature changes on TMIR have been greatly reduced by the inclusion of polystyrene radomes over the feed horn and cold sky horn.

Figure 4. Scatter plot of WVR-predicted vs. actual TMIR brightness temperature data before the bias and gain corrections are made to the TMIR calibration but after the T/V processing errors were corrected. The WVR measurements of downwelling atmospheric brightness temperature and total atmospheric opacity are used to infer the TMIR data by including a model for the ocean surface emissivity. This is done under cloudless, low wind (≤ 7 m/s) conditions to minimize model dependent errors.

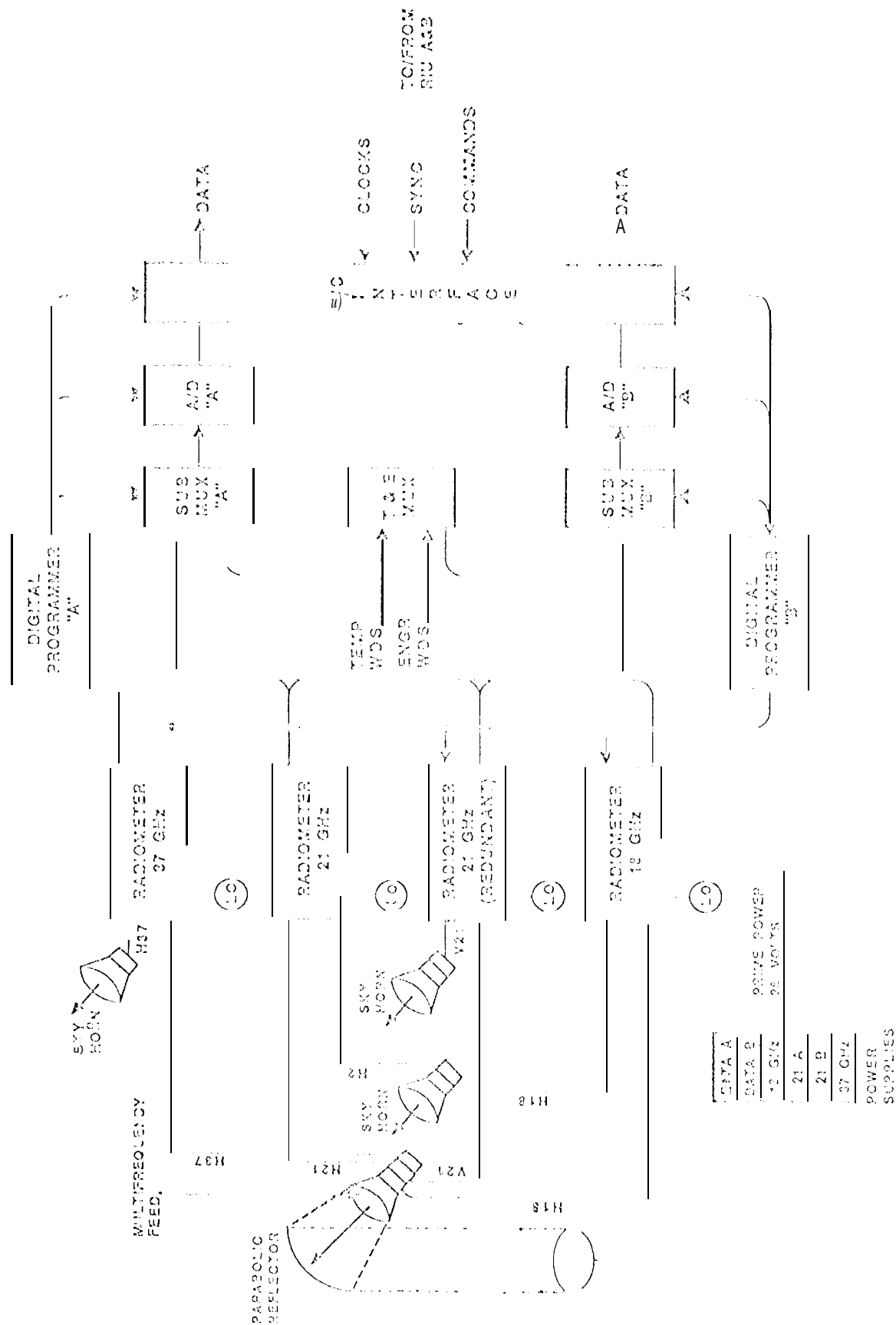
Figure 5. Scatter plot of independent sources of path delay measurements against TMIR derived path delay, with TMIR calibration in a state similar to that for Figure 4. (A) Radiosonde path delay for 268 overpasses within 100 km and 6 hours of balloon launch. Data includes all clear, calm, cloudy, and windy conditions. (B) ECMWF path delay interpolated in time and space to coincide with TMIR data. Data includes a random sample of open ocean measurements during days 290-301 of 1992 (Y/P cycle 3).

figure 6. Scatter plot of WVR-predicted vs. actual TMIR brightness temperatures after

all calibration corrections are made. The 2-3 K offsets can largely be explained by a small increase in the calm sea emissivity above that of the ideal Fresnel condition.

Figure 7. Scatter plot of TMR against radiosonde path delays for the same data set described in figure 5A, but with all the corrections to the instrument calibration and water vapor line strength incorporated into the TMR data processing.

Figure 8. Scatter plot of TMR path delay retrieval error (defined as radiosonde path delay - TMR path delay) against TMR retrievals of (A) ocean surface wind speed and (B) integrated cloud liquid water content.



TMR Instrument Temperature

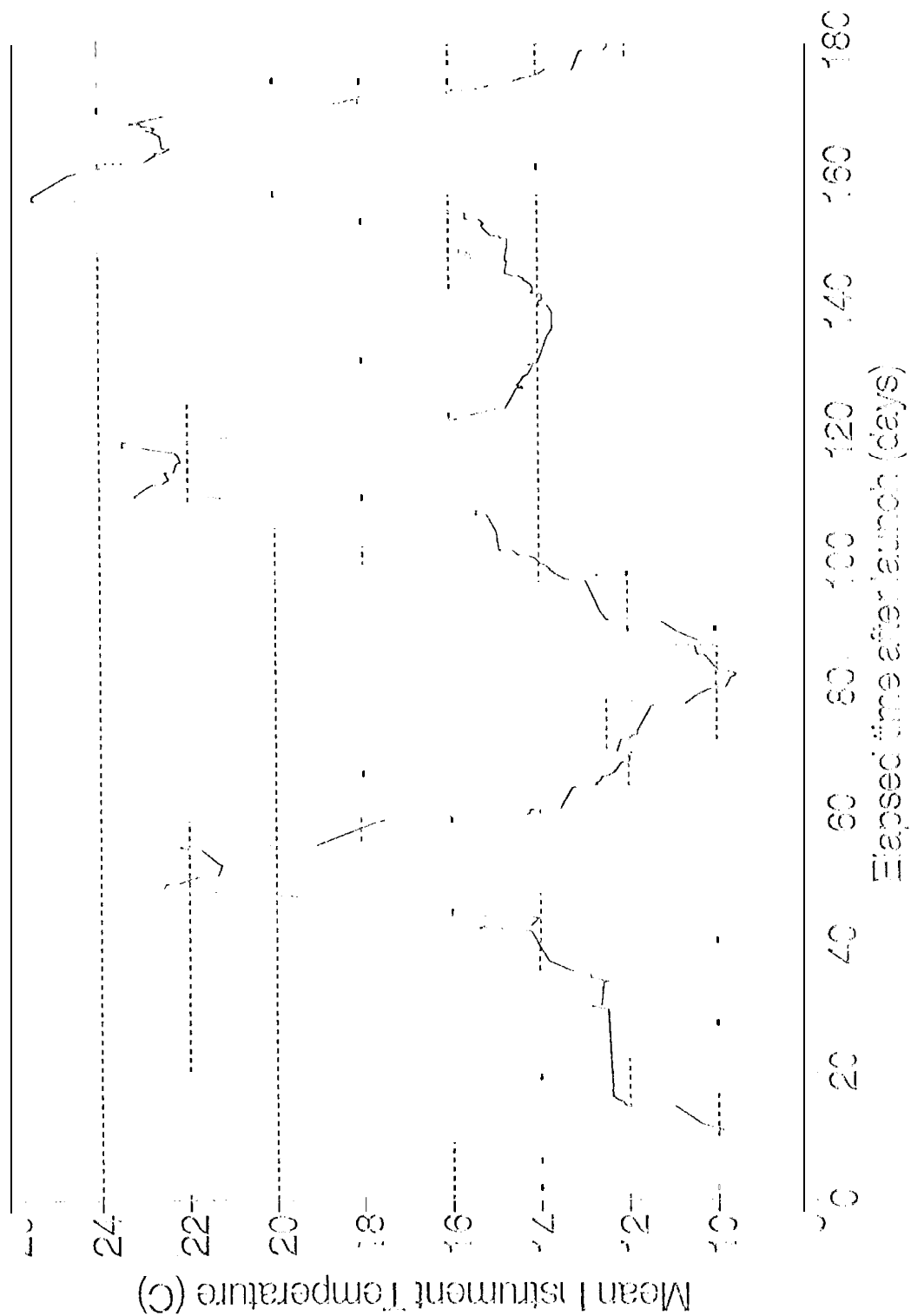


Fig 2

Nimbus-7 SVM/R Instrument Temperature Variations

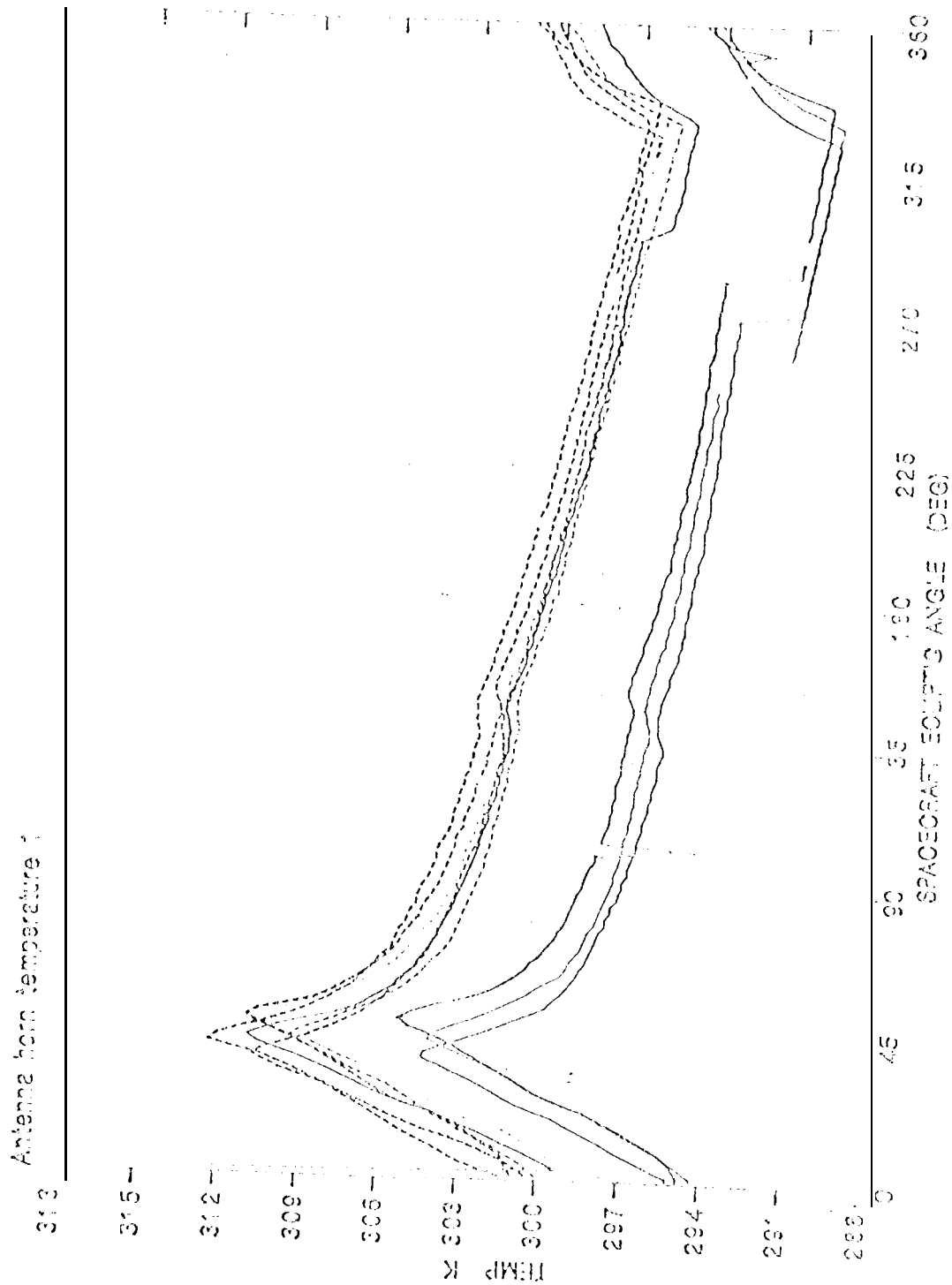
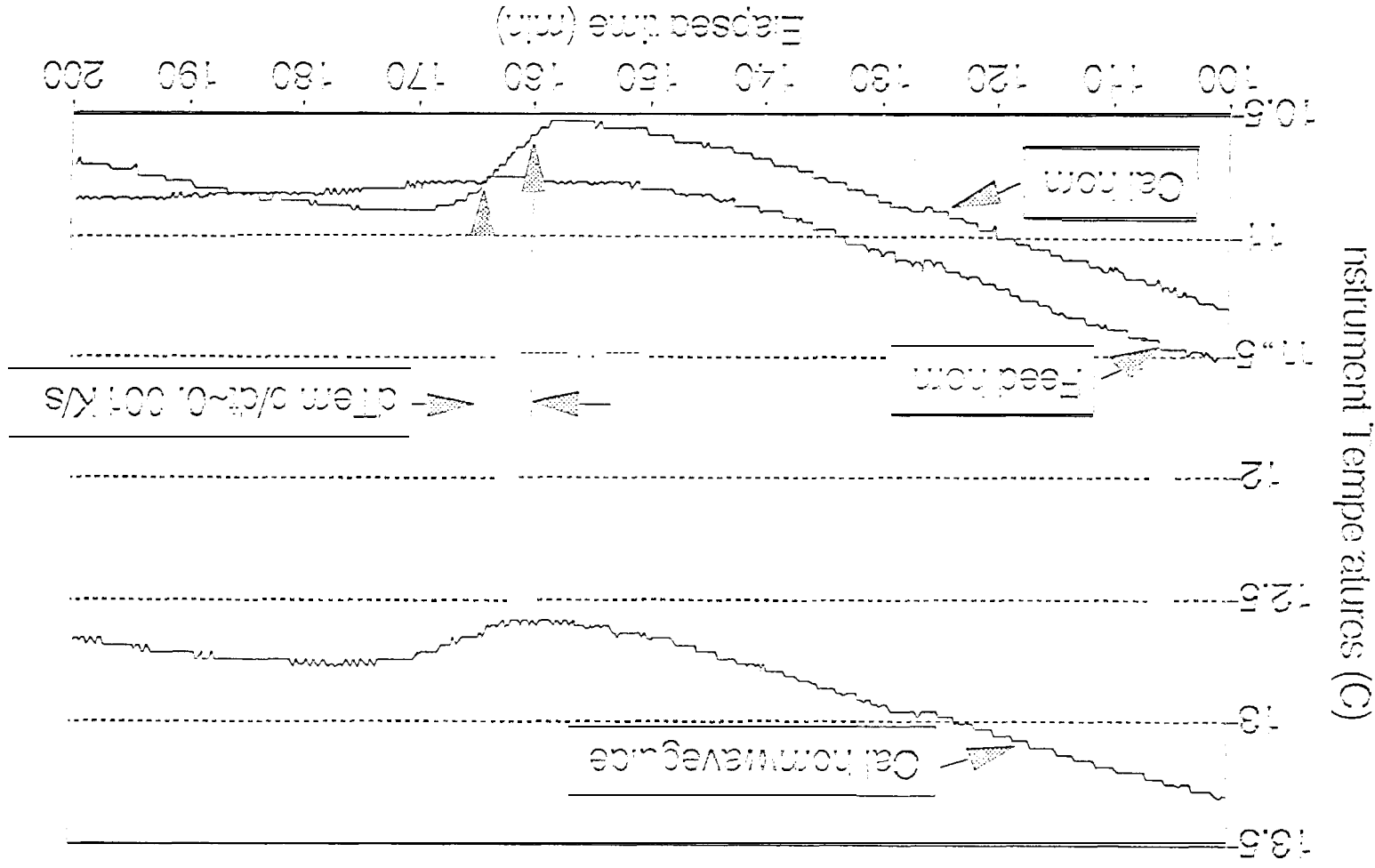


Fig 3A

TOP-EX Microwave Radiometer Day 246, September 2, 1992



TWR TB18 VS GROUND WVR PREDICTED TB18
CLEAR, CALM DATA ONLY

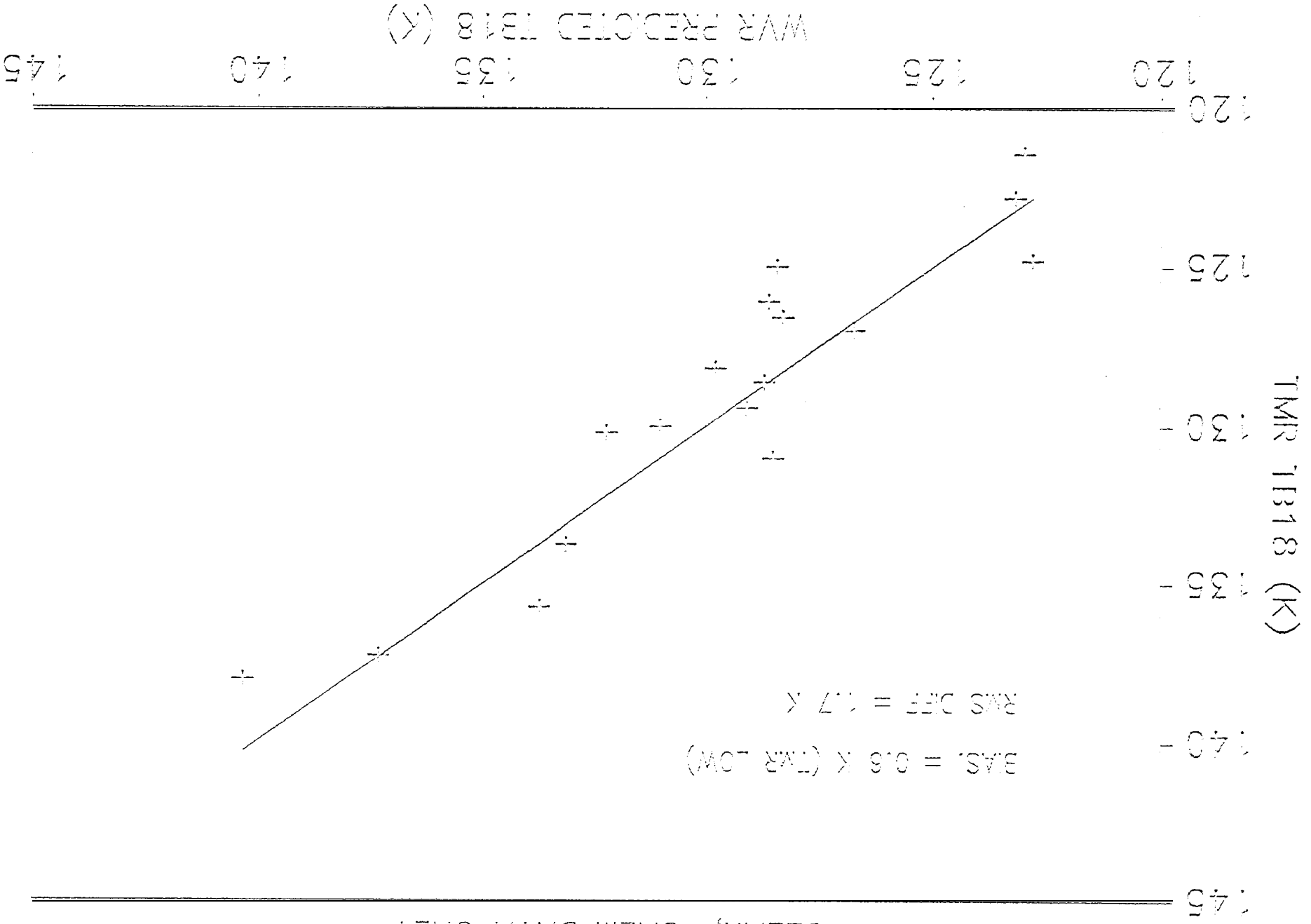
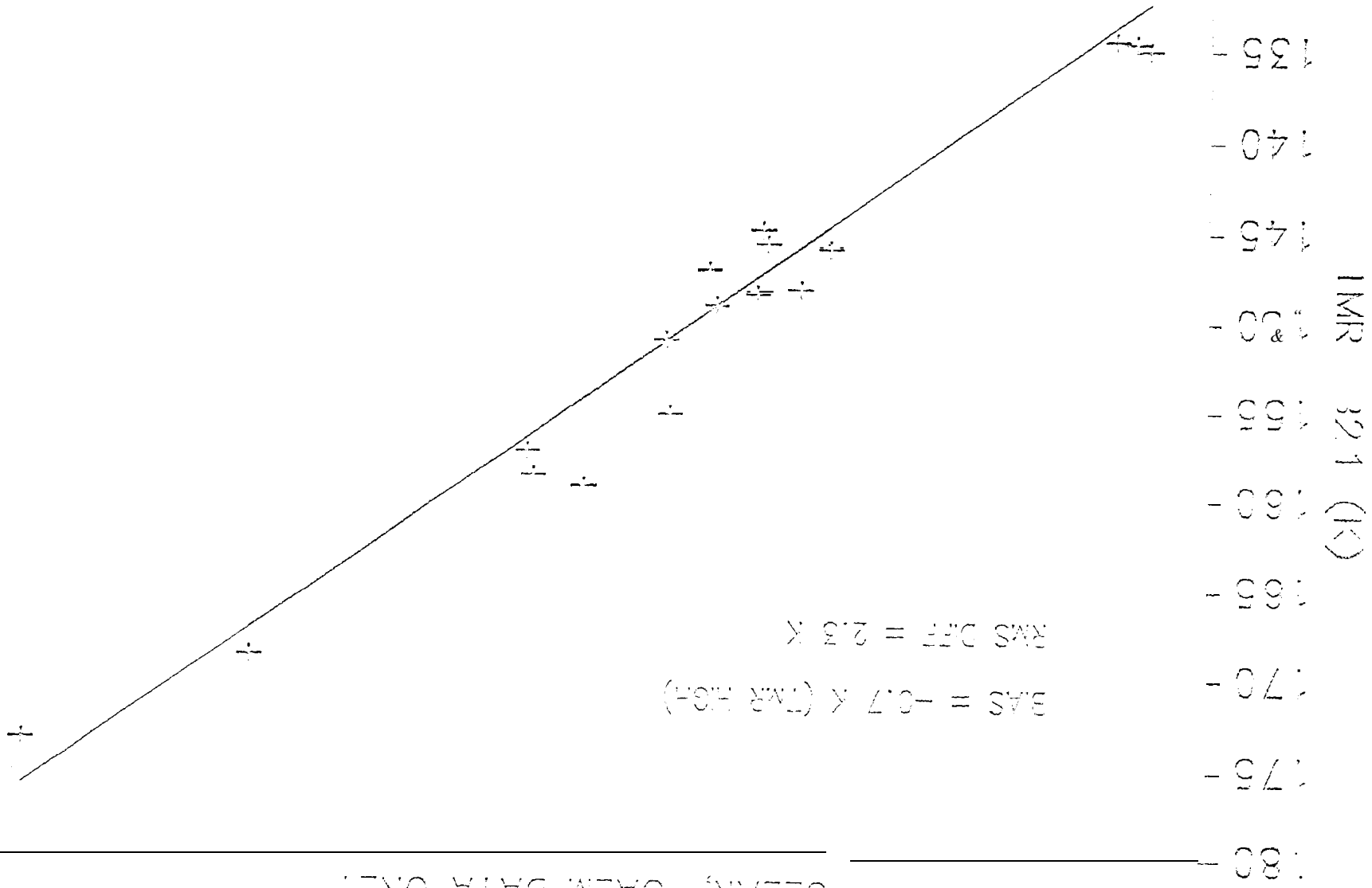


Fig 4A

TWR TB21 VS GROUND WVR PREDICTED TB21
CLEAR, CALM DATA ONLY



WVR PREDICTED TB21 (K)

130 135 140 145 150 155 160 165 170 175 180

0448

TWR 1937 VS GROUND WVR PREDICTED 1937
 CLEAR, CALM DATA ONLY



WVR PREDICTED 1937 (K)

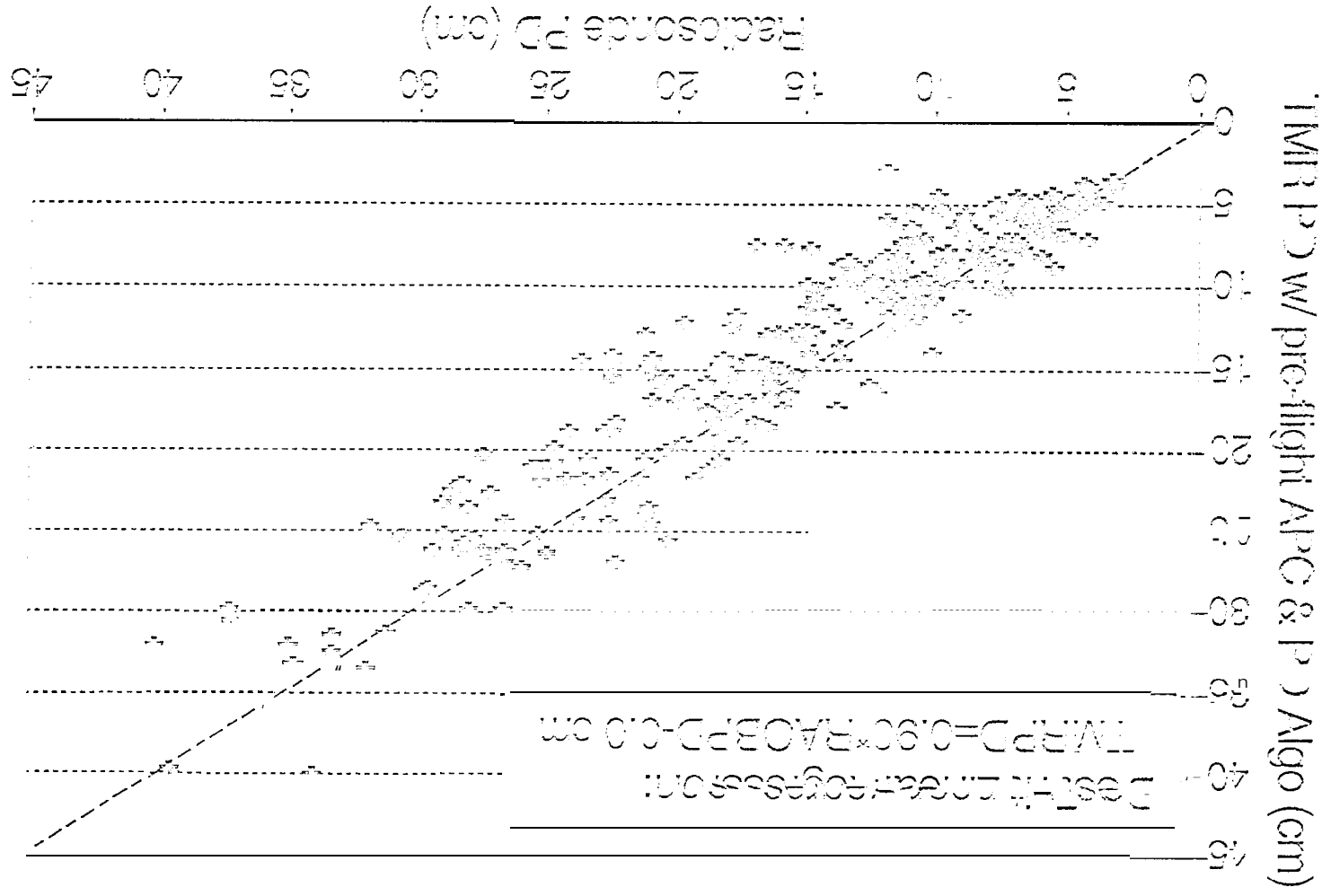
140
145
150
155
160
165
170

175
170
165
160
155
150
145

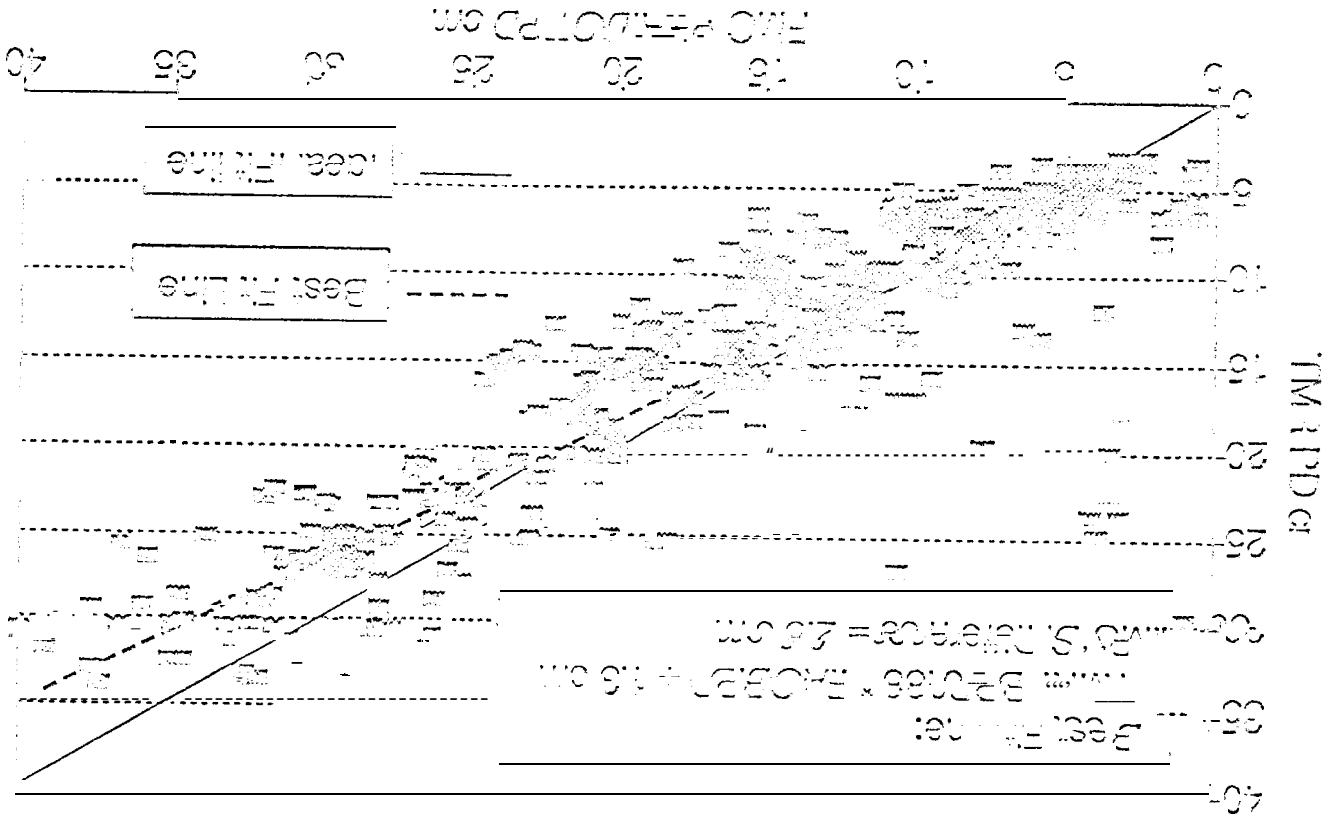
IMF 130/ (K)

24

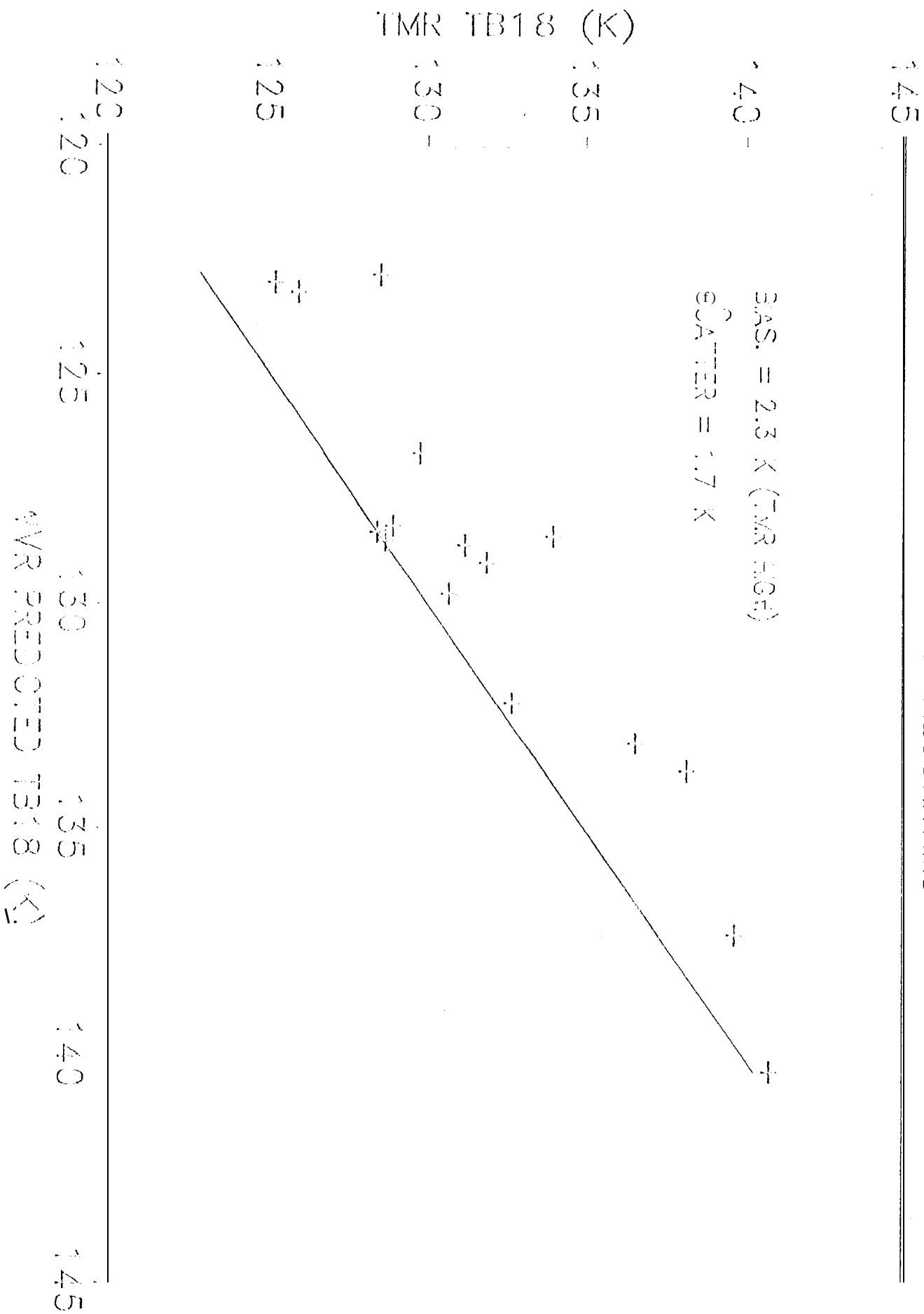
TM. V. Radiosonde Path Delay
First 6 months of mission (N=268)



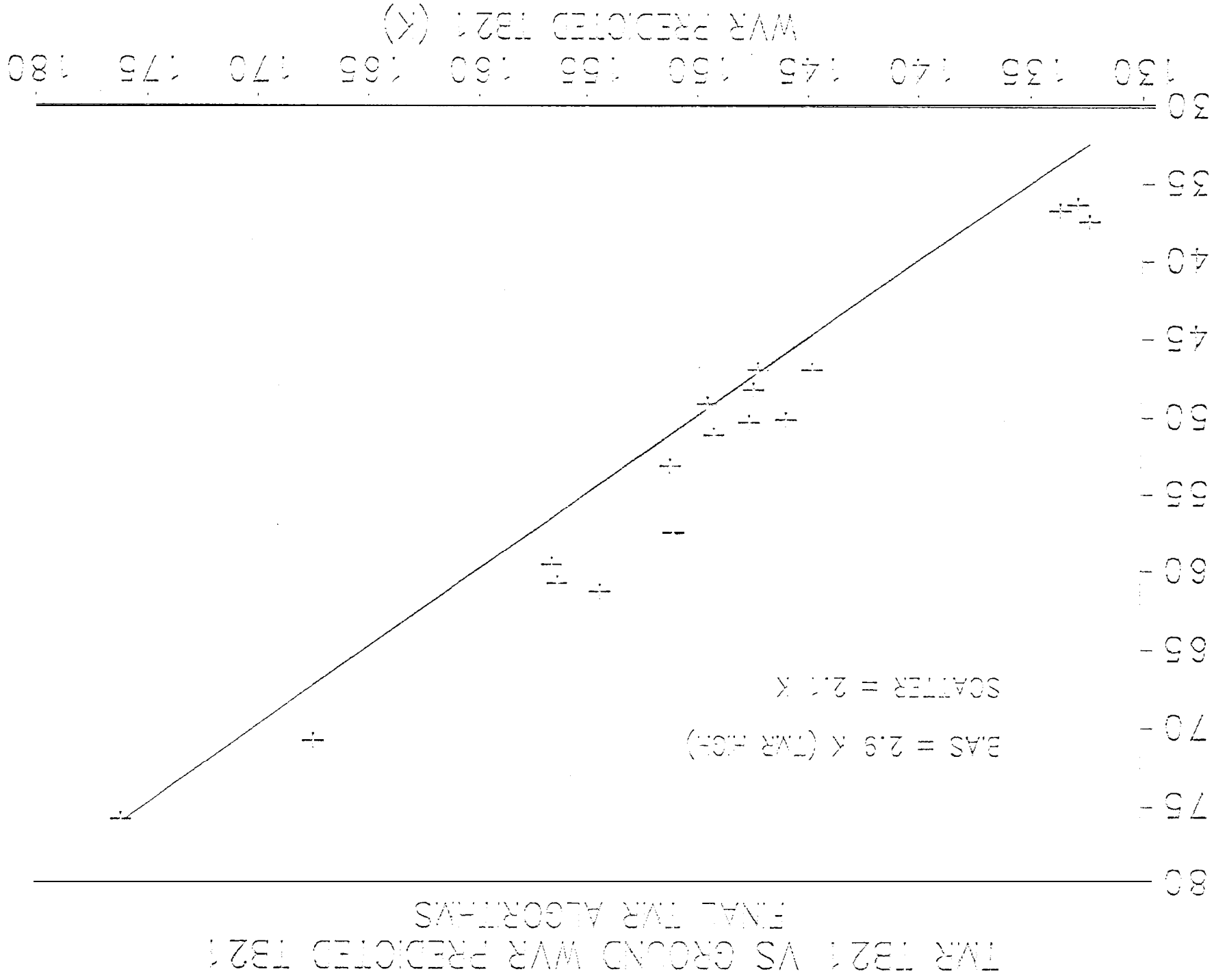
Comparison of TMR PDs Vs. FMO PD



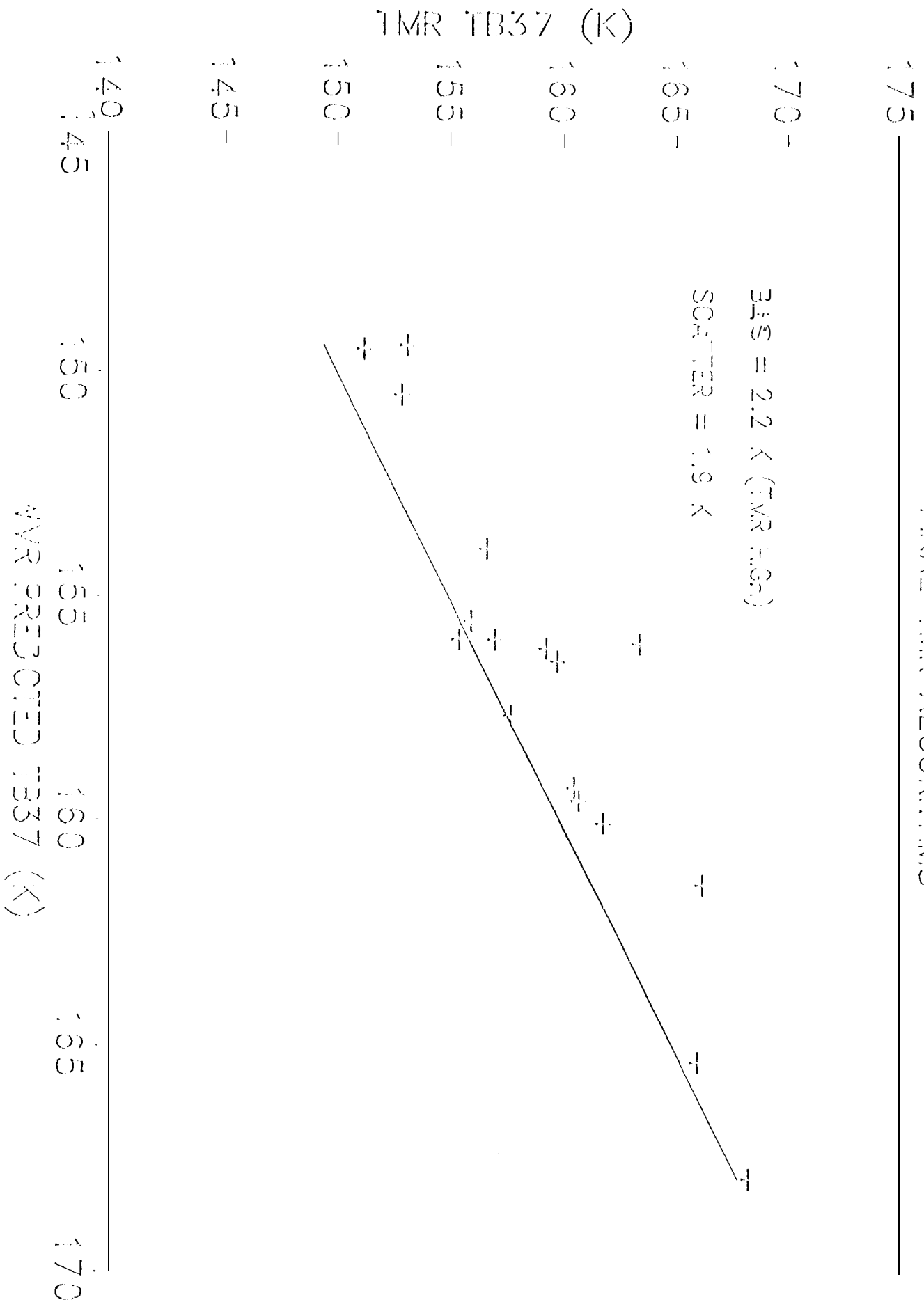
TMR TB18 VS GROUND WVR PREDICTED TB18 FINAL TMR ALGORITHMS



IMR 321 (<)



WAR 1937 VS GROUND WAR PREDICTED 1937
FINAL WAR ALGORITHMS



TM R V. Radiosonde Path Delay First 6 months of mission (N=268)

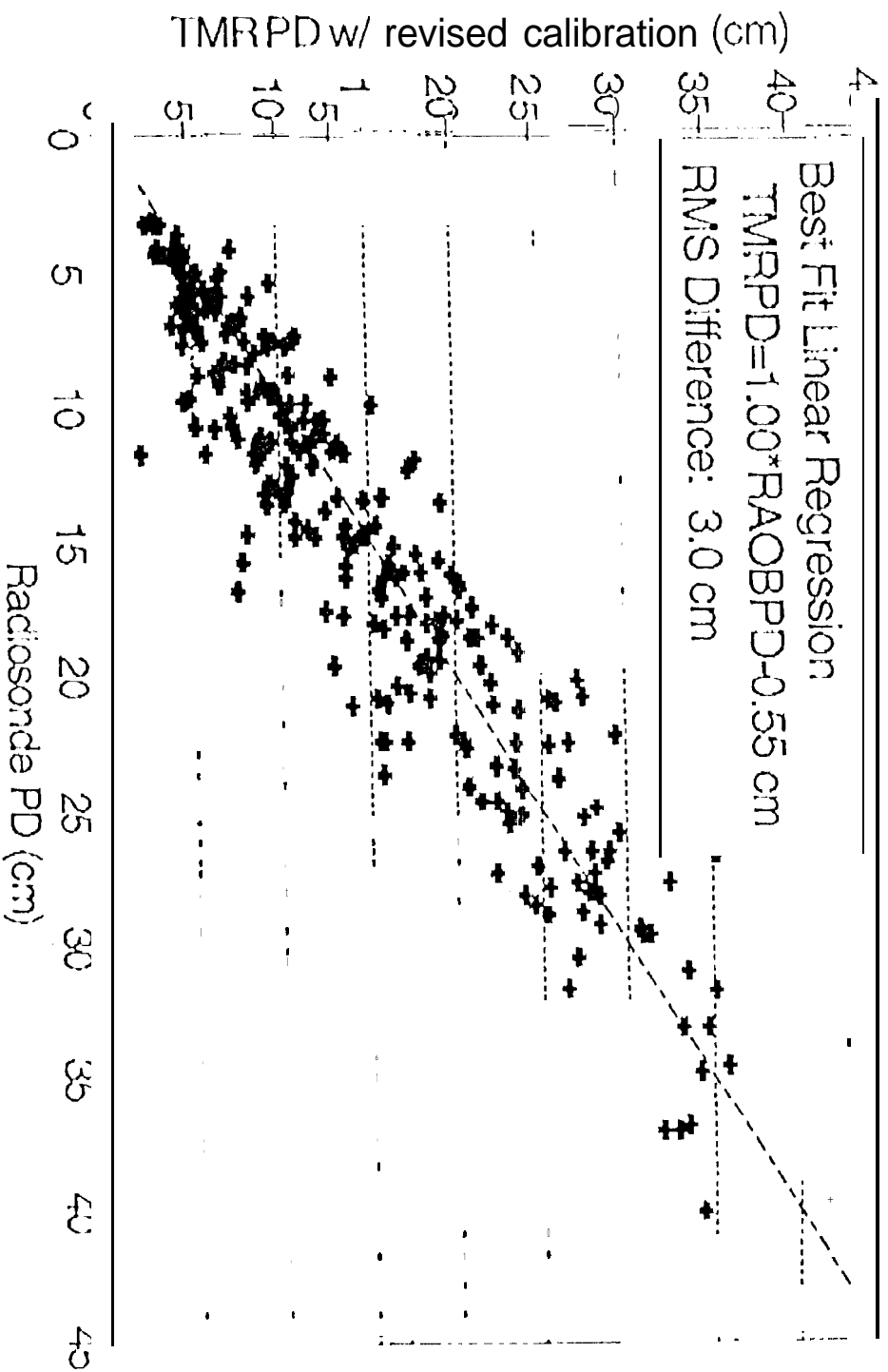


Fig. 7

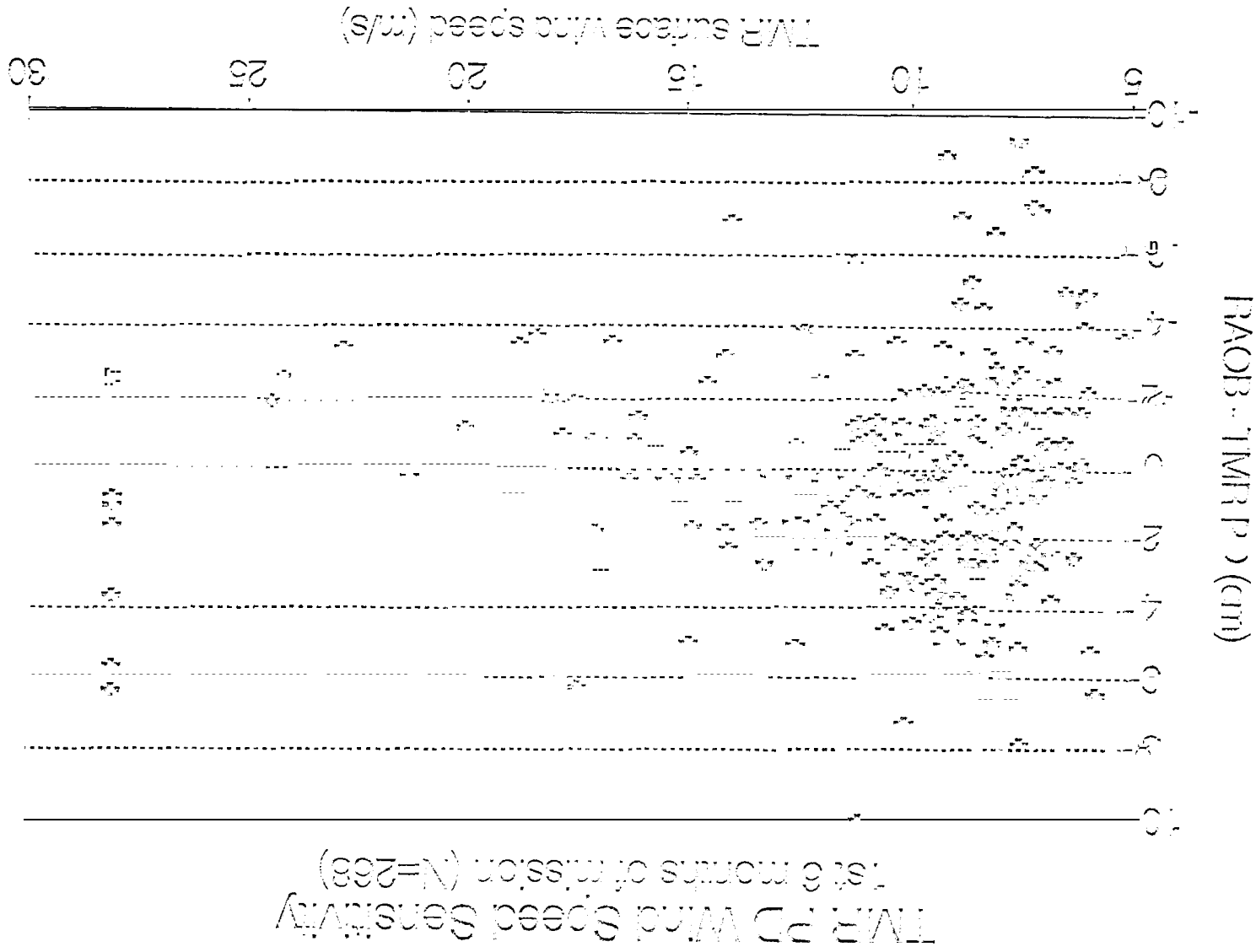
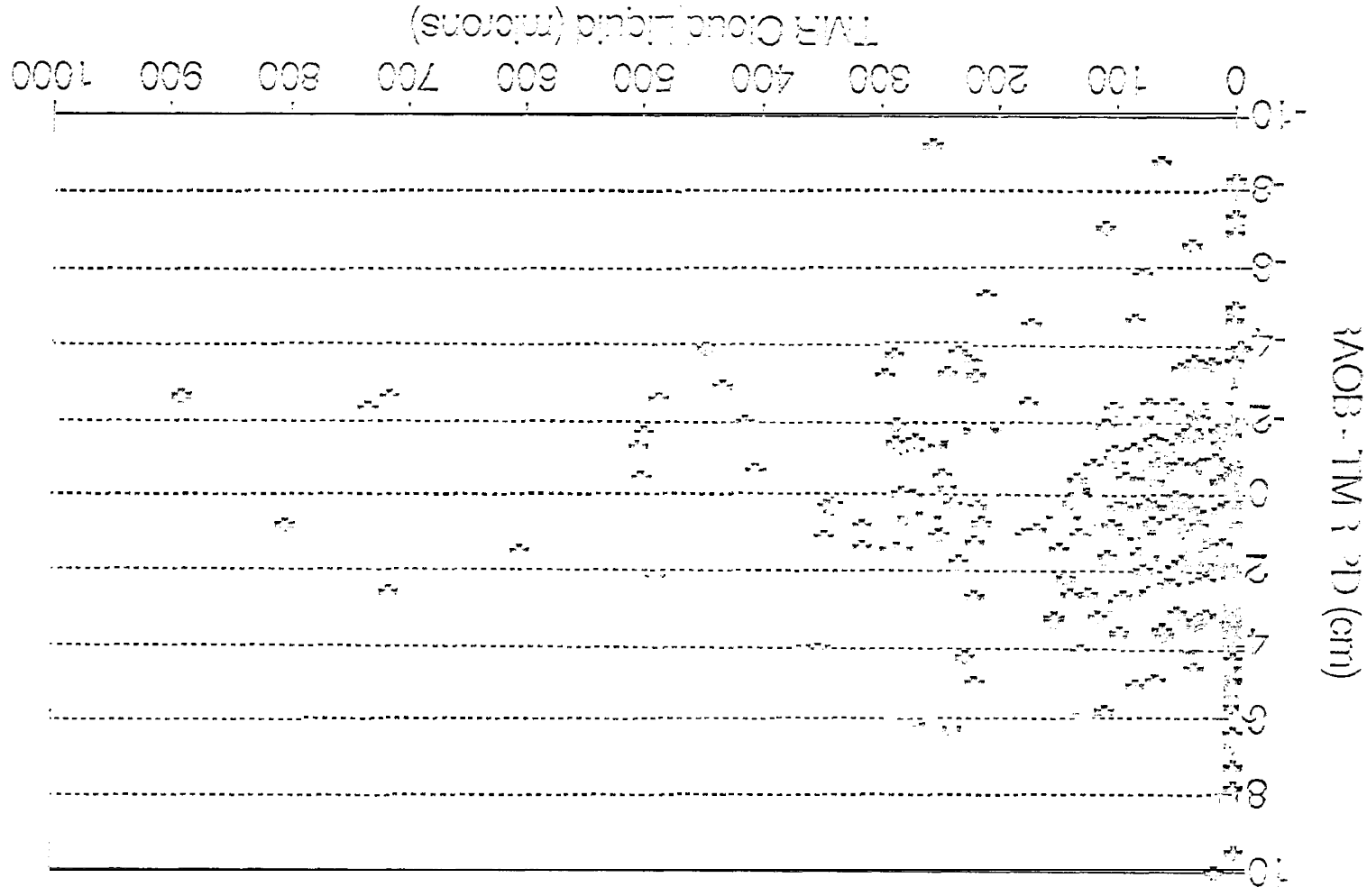


Fig 8A

TMR PD Cloud Liquid Sensitivity
1st 6 months of mission (N=268)

First 6 months of mission. (N=268)

 $\lambda_{\text{MOB-TM}}^{\text{D}} \text{ (nm)}$

TMF Cloud Liquid (microns)